Volume 13
Number 9
7 March 2025
Pages 4265–4818

Journal of Materials Chemistry C

Materials for optical, magnetic and electronic devices

rsc.li/materials-c

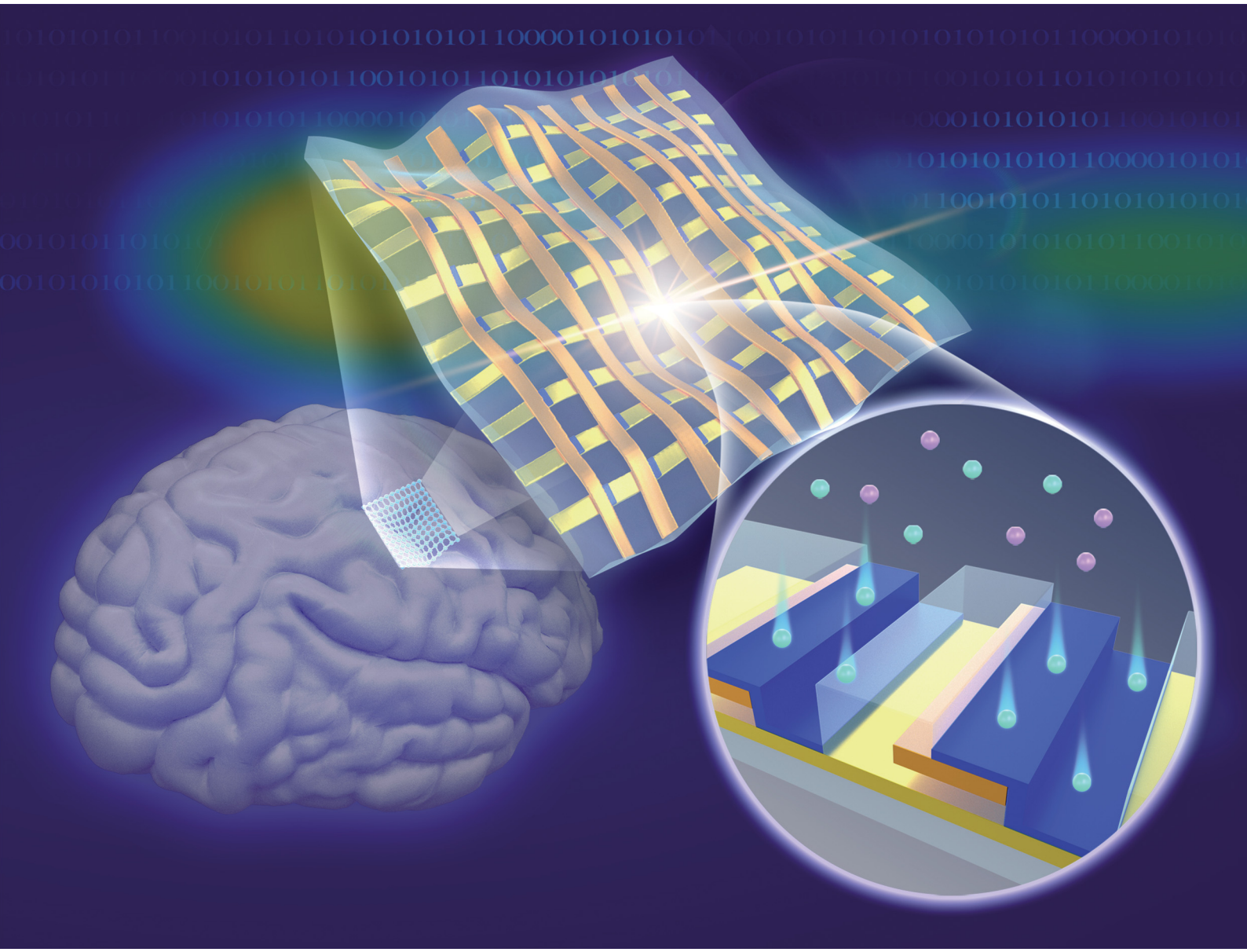

ISSN 2050-7526

ROYAL SOCIETY OF CHEMISTRY

PAPER

Xiaomin Xu *et al.*

High-density, ultraflexible organic electrochemical transistor array for brain activity mapping

Journal of Materials Chemistry C

ROYAL SOCIETY OF CHEMISTRY

PAPER

View Article Online
View Journal | View Issue

Check for updates

Cite this: J. Mater. Chem. C, 2025, 13, 4385

High-density, ultraflexible organic electrochemical transistor array for brain activity mapping†

Wei Xu,‡[a] Yanlan Zhu,‡[a] Xiaolin Zhou,‡[b] Haoyue Guo,[b] Jingxin Wang,[a] Ruiqi Zhu,[a] Zhengwei Hu,[b] Wei Ma,[c] Xing Ma,[d] Xiaojian Li[b] and Xiaomin Xu *[a]

Received 4th July 2024,
Accepted 18th January 2025

DOI: 10.1039/d4tc02839b

rsc.li/materials-c

Organic electrochemical transistors (OECTs) are emerging as promising neural electrodes due to their capabilities for on-site signal amplification, customizable mechanical flexibility, biocompatibility, and stability in biotic conditions. However, documented flexible OECT arrays face limitations in channel count and spatiotemporal resolution. Here, we report a high-density, ultraflexible OECT array designed explicitly for the high-resolution electrocorticogram (ECoG) signal recording. Featuring vertically stacked source and drain electrodes, the array incorporates 1024 channels in a compact form factor, only 4.2 μm thick, achieving a density of 10 000 transistors per square centimeter. A 16 × 16 segment of the 1024-channel array was utilized to map whisker-related signals in a mouse model, effectively locating neural activities in response to tactile stimulation. Besides, it demonstrates high mechanical compliance and long-term stability, remaining effective for three months post-implantation and beyond. With its excellent resolution and durability, the ultraflexible OECT array promises to enhance the monitoring and understanding of neural dynamics across a wide spatiotemporal scale.

Open Access Article. Published on 20 2025. Downloaded on 27.02.2026 08:34:30.
This article is licensed under a Creative Commons Attribution-NonCommercial 3.0 Unported Licence.

Introduction

The brain, a complex organ comprising approximately 86 billion neurons[1] interconnected in a neural network, performs a wide range of dynamic functions—from sensation and cognition to action—while consuming a remarkably low amount of energy, estimated at 10–20 W.[2] To achieve a system-level understanding of the brain,[3] it is essential to gather information on the spatial and temporal activation of various neuronal populations.[4–6] Electrocorticography (ECoG), which involves recording electrophysiological activities across a broad cortical area,[7] has emerged as an essential tool in this pursuit. By utilizing a minimally invasive, flexible sheet placed directly on the cortex, the ECoG technique facilitates extensive research into brain function and neural network connectivity, further guiding the development of advanced brain–computer interfaces.[8,9]

Among neural interface techniques, organic electrochemical transistors (OECTs) have emerged as particularly promising candidates for use as active ECoG electrodes. The major advantage of OECTs over passive electrodes is their capability for *in situ* signal amplification, particularly beneficial for accurately capturing low-amplitude and high-frequency signals. OECTs designed for *in vivo* applications have demonstrated continuous improvements in electrical performance, with transconductance (g_m) reaching 8.67 mS,[10] and the signal-to-noise ratio (SNR) improving to 44 dB.[11] These rapid advancements and attributes including a direct interface to bridge biological system with external electronics position OECTs an ideal choice for integration into the next generation of neural interfaces.

Mechanical flexibility is crucial for neural interfaces, as it ensures conformability with the brain's soft and curved surface, reduces potential tissue damage, and enhances long-term stability and biocompatibility.[12] Recent advancements have led to the development of flexible OECT devices on thin substrates such as polyimide, parylene, and polyethylene terephthalate (PET).[13,14] Despite these advances, several challenges remain in the fabrication and implementation of these technologies.

One critical issue with existing flexible OECT arrays is their limited spatiotemporal resolution. High-density sampling is essential for unravelling the spatial distribution characteristics of brain electrical signals, particularly for high-frequency signals,[15–18] as it enables the calculation of current source

[a] Institute of Materials Research, Tsinghua Shenzhen International Graduate School, Tsinghua University, Shenzhen 518055, China. E-mail: xu.xiaomin@sz.tsinghua.edu.cn
[b] CAS Key Laboratory of Brain Connectome and Manipulation, the Brain Cognition and Brain Disease Institute (BCBDI), Shenzhen Institute of Advanced Technology (SIAT), Chinese Academy of Sciences, Shenzhen 518055, China
[c] State Key Laboratory for Mechanical Behavior of Materials, Xi'an Jiaotong University, Xi'an 710000, China
[d] School of Materials Science and Engineering, and Sauvage Laboratory for Smart Materials, Harbin Institute of Technology (Shenzhen), Shenzhen, Guangdong, 518055, China

† Electronic supplementary information (ESI) available. See DOI: https://doi.org/10.1039/d4tc02839b

‡ These authors contributed equally to this work.

Open Access Article. Published on 20 2025. Downloaded on 27.02.2026 08:34:30.
This article is licensed under a Creative Commons Attribution-NonCommercial 3.0 Unported Licence.

density (CSD), facilitating the precise localization of specific signals.[19–21] Additionally, a rapid device response is essential for capturing transient phenomena such as action potentials, oscillatory brain activities, and the precise timing of neuronal firing patterns.[22,23] For high-density, active ECoG arrays, the transient response of the transistors—which determines the achievable switching speed—must be sufficiently short to ensure high temporal resolution.[23,24] To fully leverage the opportunities presented by these advancements, ongoing developments in OECT technology prioritize increasing the channel density and the response speed. Such advancements necessitate device architectures that are both compact and responsive.

To address these needs, a vertically configured OECT (vOECT) was developed by Kawahara *et al.* in 2013,[25] with screen-printed PEDOT:PSS on both sides of a paper or PET substrate, and the channel formed by a hole through the substrate. At that time, the channel length was measured approximately 50 μm. In 2017, M. J. Donahue *et al.*[26] introduced a step-like vOECT design that significantly reduced channel dimensions to submicron levels, thereby enhancing g_m and response speed, facilitating potential integration into high-density arrays. This design was subsequently utilized in applications such as complementary inverters for on-site bio-signal amplification[27] and arrays for monitoring the activity of islet micro-organs.[28] The configuration features a parallel stacking of source and drain electrodes, which allows for individual adjustment of transistor biases. However, it accommodates fewer than hundreds of transistors within the substrate, limiting its scalability.

A different form of vertically configured OECT, referred to as the sandwich-like vOECT, has been further developed. In this design, the channel material is encased by vertically-stacked source and drain electrodes.[29] This configuration has been integrated into high-density arrays,[30,31] achieving a remarkable density of approximately 7.2 million OECTs per cm^2. The direct exposure of metal electrodes to biological tissue makes this configuration unsuitable for *in vivo* signal recording. Effective packaging strategies are required to encapsulate the metal components while ensuring communication between the channel and the external solution. At present, a straightforward approach for constructing high-density, ultraflexible OECT arrays has yet to be established.

Furthermore, the integration of flexible front-end sensing components with rigid backend processing units may pose challenges concerning interfacial toughness and stability.[32] Addressing these challenges is crucial for enhancing the reliability and performance of flexible electronic devices in practical neural interface applications.

Here, we report a high-density OECT array featuring a density up to 10 000 transistors per cm^2 within an ultraflexible configuration. Each transistor is strategically positioned at the intersection of the source–drain leads, thereby eliminating the need for additional spacing and the use of a redistribution layer typically required in horizontal arrays. This approach simplifies the device fabrication process. The substrate and encapsulation layers are composed of 1.8 μm-thick parylene films, with a 0.6 μm parylene intermediate layer, resulting in an overall device thickness of just 4.2 μm. This ultrathin configuration allows for a minimum bending radius down to 5 μm, demonstrating exceptional mechanical compliance. For reference, the conventional platinum (Pt) electrodes used in this study have a thickness of 15 μm, and a Young's modulus in GPa level. Additionally, we have developed a specialized data acquisition circuit board and a test solution compatible with the PCI extensions for instrumentation (PXI) for multiplexing purpose. To ensure stable connections with relatively rigid backend circuitry, we utilize polyimide tape to reinforce the device ends, facilitating reliable connections through a zero-insertion-force (ZIF) connector. In our prototype demonstration, the 64-channel array is adopted for mapping epilepsy signals. This device array boasts a spatial resolution of 50 μm and a signal-to-noise ratio of 32 dB, demonstrating capability to discern current sources and sinks and showing potential for localizing abnormal brain actives *in vivo*. We further utilized a 16 × 16 section of the 1024-channel array to capture whisker-related signals, demonstrating its effectiveness in recording local neural activities.

Results and discussion

High-density, ultraflexible vOECT array

A vOECT array consisting of 1024 (32 × 32) transistors was fabricated on 1.8 μm thick parylene film (Fig. S1, ESI†), within a total substrate area of 3.26 × 3.26 mm^2, providing a channel density of 10 000 pixels per square centimetre. The array forms a two-dimensional (2D) grid by vertically stacking the source and drain electrodes (Fig. 1a), coloured in yellow and brown respectively. At each intersection of the source and drain, a vOECT is positioned, indicated by the blue segment. The channel consists of conducting poly(2,3-dihydrothieno-1,4-dioxin)-poly(styrenesulfonate) (PEDOT:PSS) pretreated with additives, *i.e.*, ethylene glycol, dodecyl phenylpropyl sulfonic acid to improve conductivity and (3-glycidyloxypropyl) trimethoxy silane to improve the channel stability. Right panel of Fig. 1a shows a zoom-in view of two adjacent pixels, illustrating both the side and top views of the vOECT. This design eliminates the need for additional space and circumvents the requirement of a re-distribution layer necessary in horizontal OECT arrays, thus simplifying the connectivity between devices and leads.

The resulting flexible array conforms closely to a brain model (Fig. 1b), accommodating its complex surface topology. The 1 : 1 scale human brain model simulates the topography of the cerebral cortex, aiming to replicate the complex pattern of gyri and sulci. The λ, representing the average distance between the peaks of adjacent gyri, is about 5 to 20 mm, and the h, indicating the vertical distance from the peak of a gyrus to the bottom of an adjacent sulcus, is about 2 to 4 mm.[40] The inset in Fig. 1b shows an SEM image of the device under bending, demonstrating a bending radius of 5 μm. The microscopic image of the array is depicted in Fig. 1c, revealing a channel width of 50 μm and 100 μm spacing between adjacent vOECTs, with an upper inset, Fig. 1c(ii), providing a magnified view to

 This journal is © The Royal Society of Chemistry 2025

Open Access Article. Published on 20 2025. Downloaded on 27.02.2026 08:34:30.
This article is licensed under a Creative Commons Attribution-NonCommercial 3.0 Unported Licence.

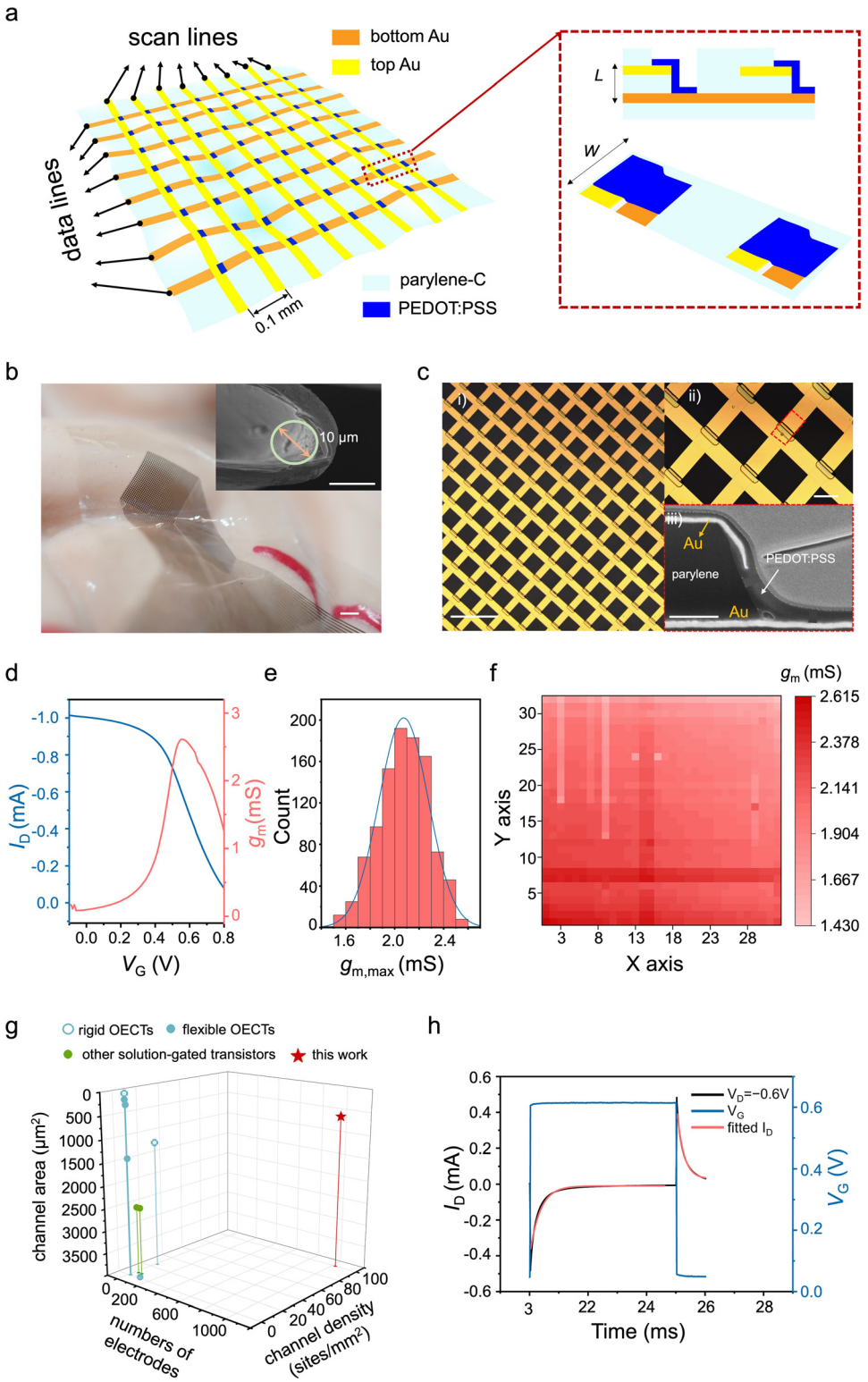

Fig. 1 Design and the performance of the ultraflexible, high-density vOECT array. (a) Left panel: Illustration of the vOECT array on a flexible parylene substrate. Right panel: Zoom-in schematics of two adjacent pixels, showing both the side view and the top view. (b) A photograph showing the ultraflexible, high-density vOECT array attached to a brain model. Scale bar, 1 mm. Inset is a scanning electron microscopic (SEM) image of a 4.2 μm-thick vOECT bent to a 5 μm radius. Scale bar, 10 μm. (c) Optical micrograph of an ultraflexible, 1024-channel vOECT array with a density of 10 000 transistors cm^{-2}. Scale bar, 200 μm. The upper inset displays a magnified image of the vOECT array (ii). Scale bar, 50 μm. The lower inset presents a cross-sectional SEM image of a vOECT (iii). Scale bar, 0.5 μm. (d) A representative transfer curve (blue) and the corresponding g_m (pink) of a vOECT. (e) Statistical distribution histograms of g_m measured for the 1024 vOECTs from an ultraflexible array. (f) A 2D map illustrating the peak g_m of the 1024 vOECTs within the array. (g) Comparison of the vOECT array layout with other documented solution-gated multiplexed arrays used for electrophysiology across three dimensions: channel count, density, and sensing area.[10,33–39] (h) Transient response measured from a typical vOECT, with V_G switching between 0 V and 0.6 V while V_D remaining at −0.6 V.

Open Access Article. Published on 20 2025. Downloaded on 27.02.2026 08:34:30. This article is licensed under a Creative Commons Attribution-NonCommercial 3.0 Unported Licence.

highlight finer structural details. The lower inset, Fig. 1c(iii), features a cross-sectional scanning electron microscopic (SEM) image of a single device, revealing a channel length of 0.6 μm and a thickness of 178 nm.

Transfer curves of 1024 transistors were tested, a representative one along with their respective transconductance curves are shown in Fig. 1d. Among the 1024 transistors, the g_m, calculated following:

$$g_m = \frac{\partial I_D}{\partial V_G} = \begin{cases} -\mu C^* \frac{Wd}{L}|V_{DS}|, & \text{for } |V_{DS}| < |V_{GS} - V_{th}| \\ \mu C^* \frac{Wd}{L}|V_{GS} - V_{th}|, & \text{for } |V_{DS}| > |V_{GS} - V_{th}| \end{cases} \quad (1)$$

where μ and C^* denote the charge carrier mobility and the volumetric capacitance, Wd/L indicates the channel geometry with W, L, and d standing for the channel width, length, and thickness, V_{th} is the threshold voltage. The calculated g_m ranges from 1.4 to 2.6 mS, yielding an average value of 2.07 ± 0.20 mS (Fig. 1e), with its transconductance distribution across the 1024-channel array shown in Fig. 1f.

Compared to existing OECT arrays and other solution-gated transistors utilized for electrophysiology, the ultraflexible vOECT array developed in this study demonstrates substantial improvements in channel number, density, and sensing area (Fig. 1g and Table S1, ESI†).[10,33–39] The transistor density achieved in this study, in particular, sets a new record among all solution-gated transistor arrays applied for electrophysiology and *in vivo*.

We further evaluated the bias stability and long-term storage stability of the OECT array. Bias stability was assessed by continuously sweeping the transfer curves a total of 80 times at a maintained drain voltage (V_D) of −0.6 V using an Ag/AgCl gate electrode (Fig. S2a, ESI†). After completing 80 cycles, the OECT retained over 92.6% of its initial drain current (I_D) and 85.9% of peak g_m (Fig. S2b, ESI†). For long-term stability evaluation, the ultraflexible OECTs were stored in ambient air and in a 0.01 M phosphate buffer saline solution (PBS), respectively, at room temperature. Transfer curves were recorded at V_D = −0.6 V from time to time. After a storage period exceeding 50 days, the devices remained more than 80% of their initial performance, specifically 81.9% of the initial peak g_m in air (Fig. S2c, ESI†) and 88.3% in PBS (Fig. S2d, ESI†). This suggests a lifetime t_{80} – defined as the duration during which the devices maintain over 80% of their initial performance—longer than 50 days. Atomic force microscopic (AFM) images revealed swelling of the devices when stored in PBS, as indicated by a slight increase in surface roughness (RMS) to 4.55 nm, compared to 3.93 nm observed in samples stored in air (Fig. S3, ESI†). Despite these morphological changes, the phase diagrams of PEDOT remained stable, with alternating phases that contribute to compact packing of PEDOT chains and maintained stable conductivity even after 51 days of immersion in PBS.

The response time (τ), defined as the duration required for the OECT to respond to an applied input signal and stabilize its output current,[41] reaches 291.3 ± 16.7 μs in our ultraflexible array, with a coefficient of determination (R^2) of 0.992. A representative temporal response curve is shown in Fig. 1h. The resulting cut-off frequency (f_T) exceeds 4 kHz, significantly surpassing the requirement for recording ECoG signals,[42] which typically occur below 500 Hz.[20]

Biocompatibility

Achieving long-term *in vivo* recording necessitates excellent biocompatibility. To validate the array's biocompatibility, we performed tests assessing both *in vitro* cytotoxicity and *in vivo* tissue immune response. Fig. 2a shows the morphology of murine hippocampal HT22 neuronal cells after exposed to 100% extracts of our vOECT array for 1 day and 5 days, compared with cells incubated solely with HT22 culture medium. There were no noticeable morphological changes in the exposed cells relative to the control group. These cells exhibited no adverse effects such as reduced growth, shrinkage, or membrane blebbing. Fig. 2b summarizes the relative cell viability after 1 day and 5 days of exposure to various concentrations of a 64 channel-OECT array extract. After 5 days *in vitro*, the relative cell viability exceeded 100% across all tested concentrations, indicating the non-cytotoxic nature of our vOECT materials.

To evaluate the tissue response elicited by the vOECT array, we implanted a 64 channel, ultraflexible OECT array onto the somatosensory cortex of C57 mice for 12 weeks. Following the implantation period, we conducted immunohistology analyses to investigate the biological reactions to the implant. We employed triple-label immunohistochemistry, utilizing antibodies against glial fibrillary acidic protein (GFAP), 4′,6-diamidino-2-phenylindole (DAPI), and ionized calcium-binding adapter molecule 1 (Iba-1) to assess the activation states of glial cells at 12 weeks post-implantation. The Iba-1 immunohistochemistry revealed the presence of both resting ramified microglia and round activated microglia beneath the control electrode (Fig. 2c). GFAP labelling, indicative of the astroglial response, recapitulated the typical response observed after cranial surgery, showing astrocytes with bifurcated morphology (Fig. 2d). DAPI is utilized to assess the presence and integrity of DNA in various cell types, which assists in evaluating cell viability and the response to treatments (Fig. 2e). Quantitative analyses of the relative fluorescence intensities for GFAP, Iba-1, and DAPI in comparison to the control group are depicted in Fig. 2f. There were no significant differences in the signal intensities of GFAP labelling of reactive astrocytes and Iba-1 labelling in the superficial layers between the two hemispheres, with values of 0.98 ± 0.01 for GFAP, 0.99 ± 0.11 for Iba-1, and 0.74 ± 0.11 for DAPI. Collectively, these findings suggest minimal cytological changes in the cortex underlying the ECoG array over the duration of the study, indicating a tolerable level of glial activity and preserved tissue integrity in response to the implanted device.

In vivo validation

We then validate the efficacy of the OECT array in ECoG signal acquisition while facilitating data processing, using a relatively lower density 8 × 8 array for signal recording and chronic

 This journal is © The Royal Society of Chemistry 2025

Open Access Article. Published on 20 2025. Downloaded on 27.02.2026 08:34:30.
This article is licensed under a Creative Commons Attribution-NonCommercial 3.0 Unported Licence.

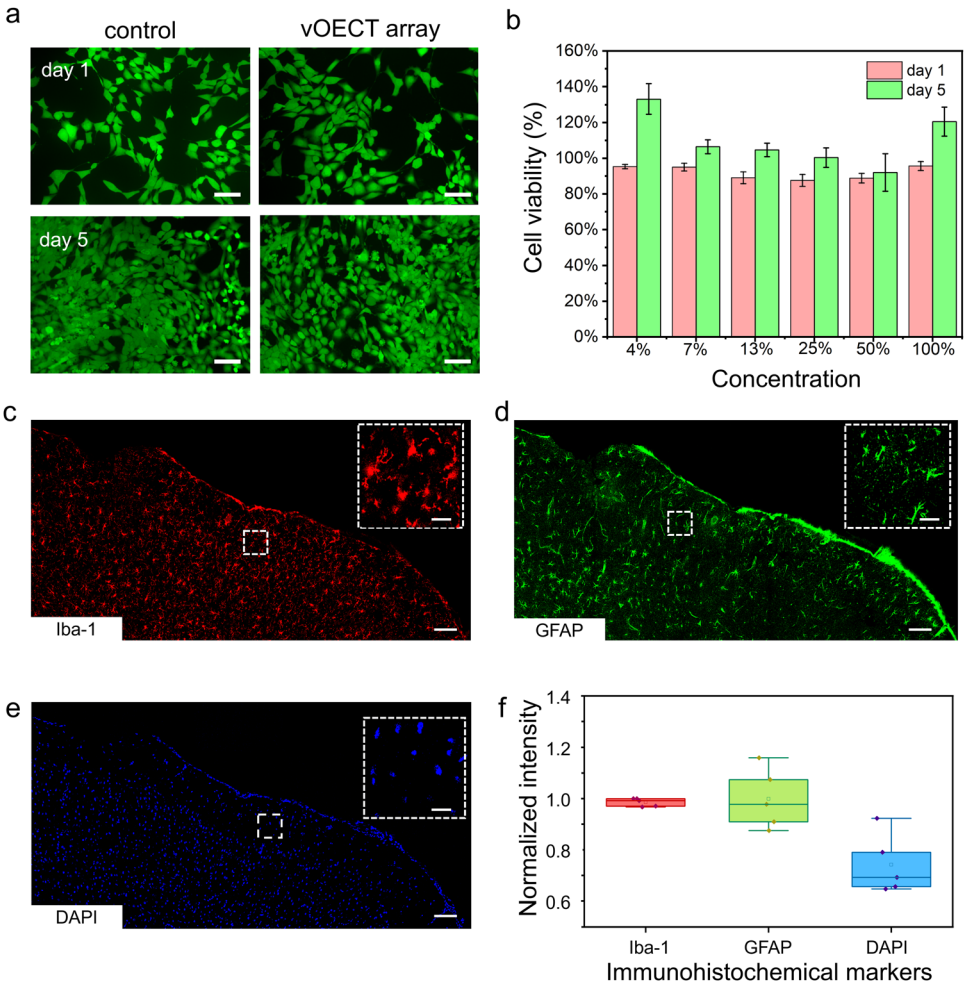

Fig. 2 *Ex vivo* biocompatibility evaluation. (a) Fluorescent images of murine hippocampal HT22 neurons cultured in bare HT22 medium and in vOECT array extract solution at 1 day and 5 days post-culture. Scale bar, 75 μm. (b) Comparison of relative cell viability on day 1 (pink) and day 5 (green) for cells exposed to different concentrations of vOECT array extract. (c) Microglia labeled with Iba-1 (red). (d) Astrocytes labeled with GFAP (green). (e) Cell nuclei stained with DAPI (blue). Insets in panels (c)–(e) display zoomed-in images showing the morphology of the labeled cells. Scale bars, 100 μm for main images; 20 μm for insets. (f) Relative fluorescence intensities of GFAP, Iba-1, and DAPI compared to the control group.

implantation. To detect multiplexed signals, a custom circuit board was designed. The schematic of the circuit board is illustrated in Fig. S4 (ESI†). Detailed designs for the circuit diagram and the PCB are found in Fig. S5–S7 (ESI†), with the system overview presented in Fig. S8 (ESI†). The drain power supply was set to −1 V, ensuring the amplifying capability of vOECT (Fig. S9, ESI†).

With a thickness of 4.2 μm and a substrate area of 1.45 × 1.45 mm^2, the 8 × 8 array features a density of 2500 transistors per cm^2. The electrical performance of the 64-channel array is detailed in Fig. S10 (ESI†), showing highly uniform characteristics, with an average g_m of 4.19 ± 0.26 mS and response time of 291.3 ± 16.7 μs.

Possessing excellent mechanical flexibility, the ultrathin vOECT array can be closely attached onto the brain of a C57 mouse (Fig. 3a) without causing trauma. The high density of the array allows all 64 sensing sites to be concentrated within a small region of the somatosensory cortex (Fig. 3b). To evaluate the recording capabilities of the vOECT array in comparison to conventional technologies, we implanted a commercial NeuroNexus ECoG array on the cortical surface of the contralateral hemisphere in the same C57 mouse (Fig. 3a). The reference array consists of 32 circular Pt electrodes, each measuring 50 μm in diameter, with a substrate area of 1 × 2.2 mm^2 (1111 electrodes per cm^2). This configuration enabled the simultaneous recording of identical seizure activity,[43] ensuring a direct comparison between signal quality of the two systems.

The temporal coincidence of the peaks in the signal trajectories demonstrates that the vOECTs capture the same information as the passive Pt electrodes,[11] as depicted in Fig. 3c and d. These figures display the average traces recorded by 64 vOECTs (Fig. 3c) and 32 Pt electrodes (Fig. 3d), capturing typical seizure-like spiking activity induced by bicuculline.[44,45] This activity is characterized by high-frequency sharp waves or rapid discharges, accompanied by slower waves in the range of 0.5–4 Hz.[46] Time-frequency analysis revealed the presence of high-frequency spikes up to 40 Hz (Fig. 3c and d, bottom panels) and demonstrated the capability of vOECTs to detect low-amplitude signals that may be

Open Access Article. Published on 20 2025. Downloaded on 27.02.2026 08:34:30.
This article is licensed under a Creative Commons Attribution-NonCommercial 3.0 Unported Licence.

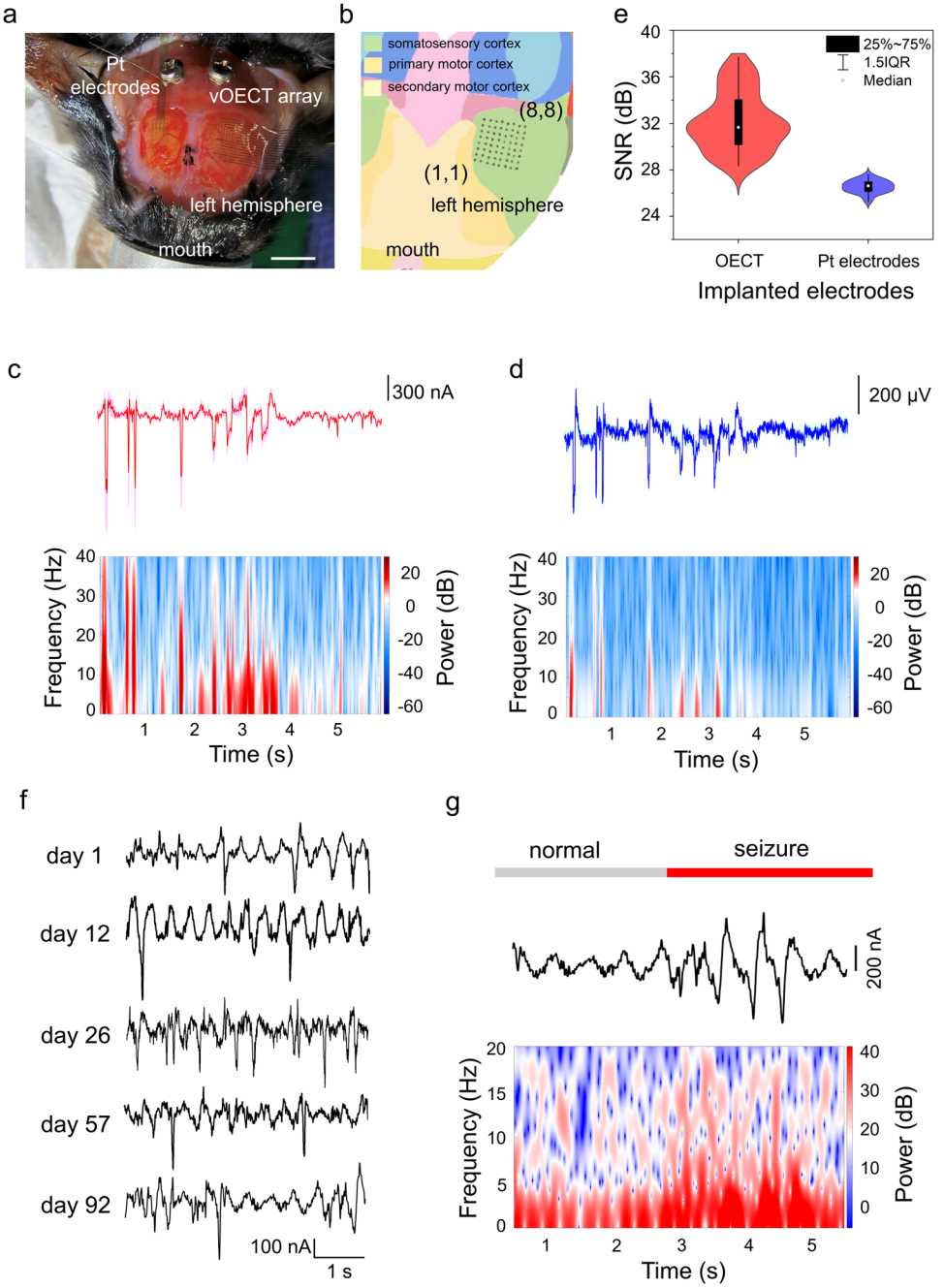

Fig. 3 *In vivo* device performance and long-term implantation stability. (a) Intraoperative photograph of the 64-channel vOECT array and a 32-channel Pt electrode array positioned on the cortical surface of the left and right hemispheres of a mouse. Scale bar, 3 mm. (b) Schematic depicting the functional areas of the brain and the locations of the vOECT biosensors, as shown in the brain atlas. The somatosensory cortex is highlighted in green, while the primary and secondary motor cortices are indicated in yellow and light-yellow, respectively. (c) Signal trajectories captured by 64 vOECTs (above) together with the corresponding time-frequency analysis plot (below). (d) Signal trajectories recorded by the 32 Pt electrodes (above) together with the corresponding time-frequency analysis plot (below). (e) Violin plot combined with a boxplot illustrating the superior SNR exhibited by the vOECTs compared to the passive Pt electrodes. The light red and blue shading represent the standard deviation bars for the vOECTs (n = 64) and Pt electrodes (n = 32), respectively. (f) Representative seizure signals recorded by the vOECT array on days 1, 12, 26, 57 and 92 post-implantation. (g) Raw LFP trace (top) and corresponding spectrogram (bottom) from the vOECT array, implanted for long-term monitoring on day 92, highlighting both normal and seizure states.

less discernible with Pt electrodes. The enhanced sensitivity of OECTs can be attributed to the inherent amplification properties, which contrasts with the passive Pt electrodes that require external amplification. As a result, the connecting leads and interfaces of the Pt electrodes collect and amplify not only the biological signals but also any associated noise, negatively impacting the SNR. The statistical results, presented in Fig. 3e, indicate that the average SNR for the 64 OECTs is 32.13 ± 2.51 dB,

 This journal is © The Royal Society of Chemistry 2025

Open Access Article. Published on 20 2025. Downloaded on 27.02.2026 08:34:30.
This article is licensed under a Creative Commons Attribution-NonCommercial 3.0 Unported Licence.

higher than that of the Pt electrodes, measured at 25.54 ± 0.55 dB. The SNR for each device was calculated by measuring the highest peak during a period of epileptiform activity relative to the standard deviation (STD) of the background during a period of low biological activity, as described in the equation below:[11]

$$\mathrm{SNR} = 20 \times \log_{10}\left(\frac{A_{\mathrm{signal}}}{A_{\mathrm{noise}}}\right)(\mathrm{dB}) \quad (2)$$

where A_{signal} refers to the amplitude of highest peak observed during epileptiform activity, A_{noise} represents the amplitude of noise, indicated by the STD of the background signal during low biological activity. For OECTs, the highest observed peak was 863.34 nA, with a background STD of 19.66 nA, resulting in an SNR of 31.65 dB. The Pt electrodes displayed a peak of 430.54 μV and a background STD of 20.28 μV, yielding a lower SNR of 26.53 dB.

Long-term application stability

We subsequently implanted the ultraflexible, 64-channel array onto the mouse cerebral cortex for long-term evaluation of its recording capabilities (Fig. S11, ESI†). Fig. 3f shows representative seizure activity signals captured by the vOECT on days 1, 12, 26, 57, and 92 post-implantations. All recordings exhibit characteristics of high-frequency sharp waves and fast discharges, accompanied by slow waves.[47] Analysis of the waveforms reveals that the amplitudes of the signals recorded on day 92 remain comparable to those observed on days 1, 12, 26, and 57. Fig. 3g presents a typical data trace along with the corresponding spectrogram recorded on day 92, illustrating the transition of ECoG signals from a normal state to an epileptic state induced by bicuculline. During such transition, there was a notable increase in signal intensity, particularly within the high-frequency range of 15–30 Hz, indicating a general upsurge in neuronal activity during the epileptic event.[47] The consistent ability to record such signals over a chronic period underscores the reliability of the neural interface and the well-being of the surrounding neural tissue. The observations above suggest that the ultraflexible, high-density vOECT array can maintain functional integrity over an extended period of up to three months, capable of chronic applications.

Neural signal mapping using high-density vOECT array

We then demonstrate the high spatial resolution of ECoG signal acquisition using a 16 × 16 segment of the ultraflexible, 1024-channel vOECT array, which has a density of 10 000 sites per cm^2. The evaluation employs both epileptic signals and externally induced whisker models, utilizing a PXI system as the acquisition platform.

Notably, ungrounded leads typically result in significant crosstalk, where current from adjacent channels affects the signals at the monitored sites[48] (Fig. S12a and b, ESI†). On the other hand, grounding had a minimal impact on the g_m (Fig. S12c, ESI†). By covering non-target transistor sites with NaCl droplets during testing of the target transistors, we show that grounding effectively reduces crosstalk (Fig. S12d—f, ESI†). Therefore, to minimize crosstalk in our high-density array, we grounded all floating lines during *in vivo* measurements using the PXI setup. The schematic of the PXI setup is shown in Fig. S13 (ESI†). The PXIe-7858 and PXIe-7866 modules were used to pulse the drain voltage, while the PXIe-4309 and PXIe-6289 modules were used to record data from the source and drain columns. The sampling rate were adjusted through the PXI setup. We selected a sampling frequency of 250 Hz for capturing epileptic signals and 625 Hz for whisker-related signals. The choice is based on the Nyquist—Shannon sampling theorem, which states that the sampling rate must be at least twice the highest frequency component of the target signal to accurately reconstruct it.

Fig. 4a illustrates the placement of the high-density device for seizure signal mapping, highlighting the selected recording sites. The exact position of the ECoG array on the mouse cortical surface is depicted in the photograph (Fig. 4b), which focuses on signals from the right frontal cortex region. This region is situated 2 mm anterior to the bregma in the anterior–posterior (AP) direction and 2 mm in the medial-lateral (ML) direction. During epileptic seizures, the energy of the recorded signals was integrated to generate a mapping visualization (Fig. 4c). Detailed waveforms of the epileptic signals from selected channels are presented in Fig. 4d, where a comparison between normal and epileptic states confirms the successful establishment of the epilepsy model.

We further demonstrate the mapping of whisker-related neural signals using a different 16 × 16 segment from the 1024-channel vOECT array positioned over the barrel cortex (schematic illustrated in Fig. 5a). Whiskers are essential sensory organs for mice, enabling them to navigate their environment, forage for food, and engage in social interactions.[49] Understanding whisker-related ECoG signals is crucial for investigating sensory processing, neural circuitry, and behavioural responses.[50] To detect the signals associated with external-induced whisker deflection, the high-density vOECT array was positioned on the mouse cortex at a location 1.5 mm posterior to bregma in the AP direction and 3 mm in the ML direction within the barrel cortex (Fig. 5b). Energy mapping prior to whisker deflection is shown in Fig. 5c, while the maps following whisker flicking, recorded at 0.02 s intervals, are displayed in Fig. 5d. Each map shows the total energy summed over signals within a 0.02 s interval, illustrating the strengthening and subsequent diminishing of signals over time. The waveforms from selected locations within the high-density array are presented in Fig. 5e. Points with stronger energy, such as channels (7,7) and (8,8), exhibit more pronounced signal fluctuations during the whisker flicking. The precise mapping of neural signals related to whisker flicking demonstrates that the OECT array can effectively detect low-amplitude signals, with the potential for future applications in the accurate localization of specific brain activity signals.

Conclusions

We report an ultraflexible, high-density vOECT array designed with vertically stacked source and drain electrodes. *In vivo*

Open Access Article. Published on 20 2025. Downloaded on 27.02.2026 08:34:30.
This article is licensed under a Creative Commons Attribution-NonCommercial 3.0 Unported Licence.

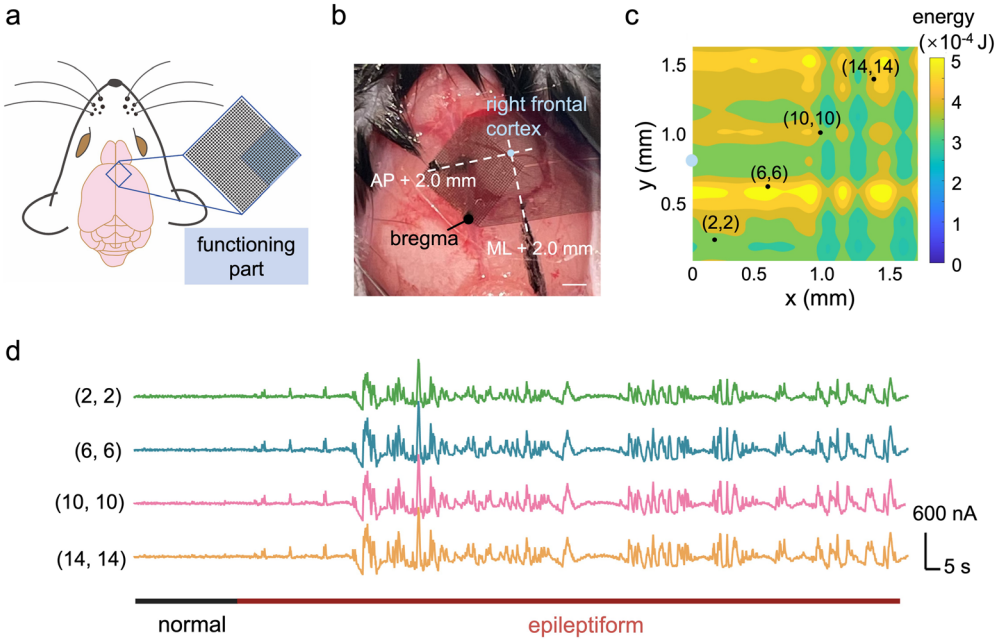

Fig. 4 High-resolution mapping of epileptic signals using ultraflexible, high-density vOECT array. (a) Schematic illustrating the placement of the high-density OECT array on the mouse cortical surface, highlighting the selected 16 × 16 array region for signal acquisition. (b) Photograph of the OECT array positioned on the mouse cortex, showing the specific brain region covered by the device, with anterior–posterior (AP) and medial-lateral (ML) coordinates labeled. Scale bar, 1 mm. (c) Mapping of signal energy across the 16 × 16 OECT array during an epileptic seizure. (d) Representative signals recorded from selected vOECT sites, displaying waveforms before and during the onset of the epileptic seizure.

validation, including the mapping of epileptic and whisker flicking signals in murine models, revealed a superior SNR and enhanced spatial resolution compared to conventional electrodes. This advancement yields a more nuanced understanding of the spatial characteristics associated with epileptic and whisker-related events. The ultraflexible vOECT array offers excellent conformability and biocompatibility, as evidenced by its ability to maintain efficient recording of cerebral electrical activity for 92 days post-implantation and beyond. The extended functionality and stability pave the way for precise monitoring of neural dynamics, laying the groundwork for ongoing advancements in neurophysiological research methodologies.

Experimental methods

Device fabrication and characterization

The schematic of device fabrication process is shown in Fig. S1 (ESI†). A parylene-C film, 1.5 μm in thickness, was first deposited onto the cleaned glass slides using an SCS parylene coater (PDS2010 LACOATOR), with poly(*p*-xylylene) (Galentis) serving as the precursor. Following the ultrathin substrate fabrication, metal pads and leads as source and drain electrodes were patterned by an optimized bilayer lift-off process. The LOR 3A (Kayaku Advanced Materials) was spin-coated onto the prepared substrate at 2500 rpm for 45 s, followed by soft-baking at 180 °C for 5 min. After cooled to room temperature, the positive photoresist S1813 (Kayaku Advanced Materials) was spin-coated at 3500 rpm for 45 s. It was then soft-baked at 115 °C for 60 s and exposed to 365 nm UV light with a dose of 70 mJ cm^{-2} using the URE-2000/35AL system. The photoresist was developed in ZX-238 developer (Jianghua Micro) with manual agitation for 60 s, followed by rinsing with de-ionized (DI) water and drying with a nitrogen gun. Residual organic contaminants present on the substrate surface were removed using an oxygen plasma treatment (Atto-BL-PCCE, Diener electronic). Subsequently, a 5 nm chromium layer followed by a 50 nm gold layer were thermally evaporated onto the substrates using a vacuum thermal evaporator (Nexdep, Angstrom Engineering). To strip the resist, the devices underwent a soaking process in remover 1165 media (Jianghua Micro) for 20 minutes at 60 °C, with manual agitation by pipetting. The substrates were then rinsed twice with ethyl alcohol and DI water, and dried using a nitrogen gun. Following the initial electrode deposition, a 1.2 μm-thick parylene film was deposited onto the slides, serving as an intermediate layer to isolate the upper and lower electrode layers and define the channel length. Next, a second layer of metal was patterned on this layer of parylene to serve as the drain electrode, cross overlapping with the bottom layer of metal to create the vertically stacked source and drain contacts and following a process analogous to the fabrication of the first layer metal lines. Subsequently insulating and sacrificial layers of parylene were deposited, both to a thickness of 1.8 μm. Before depositing the sacrificial parylene layer, a diluted solution of the industrial cleaner Micro-90 (1 : 20 by weight) was spin-coated onto the insulating parylene layer as an anti-adhesion layer. This facilitated the later removal of the sacrificial layer from the encapsulation layer, thereby defining and

 This journal is © The Royal Society of Chemistry 2025

Open Access Article. Published on 20 2025. Downloaded on 27.02.2026 08:34:30.
This article is licensed under a Creative Commons Attribution-NonCommercial 3.0 Unported Licence.

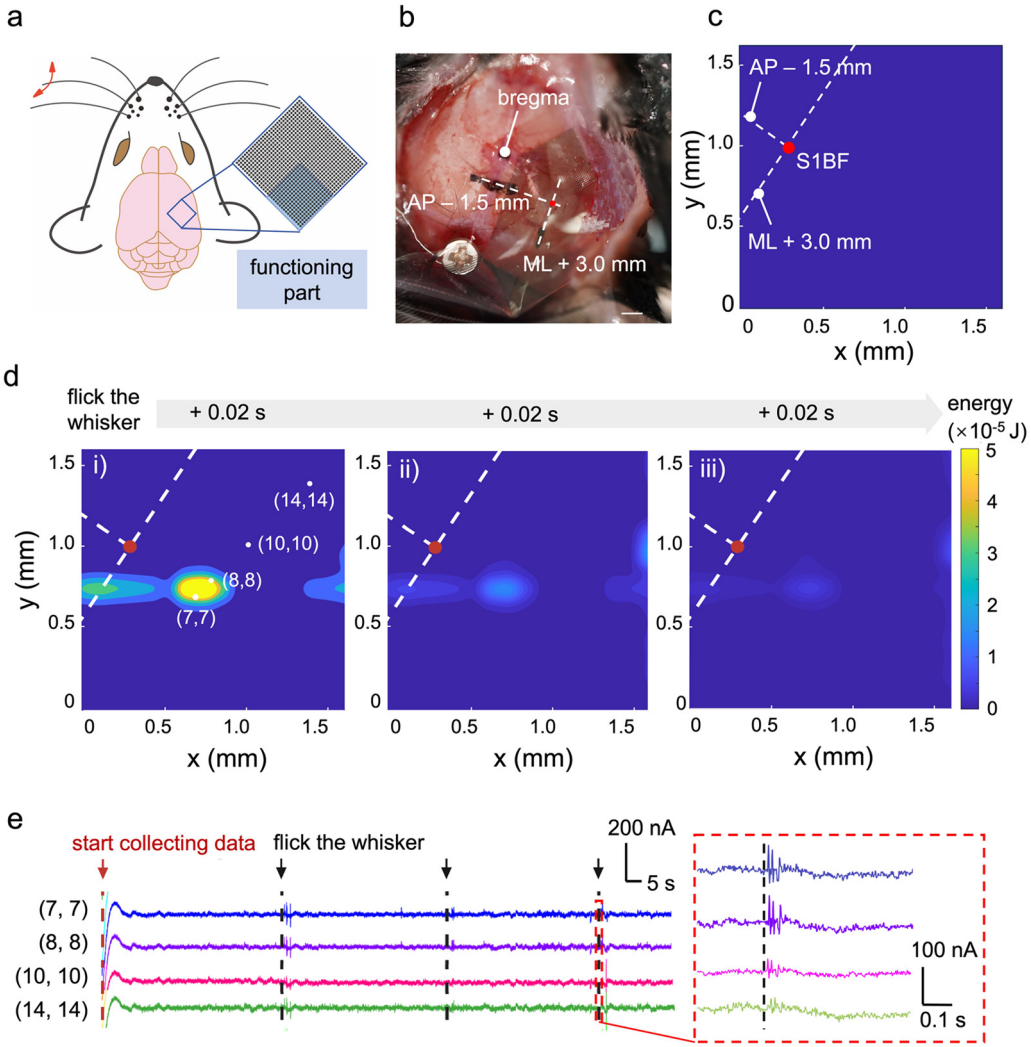

Fig. 5 High-resolution mapping of whisker flicking signals using an ultraflexible, high-density vOECT array. (a) Schematic of the vOECT array positioned on the mouse cortex, highlighting the selected working devices. (b) Photograph of the implanted OECT array on the mouse cortex, with AP and ML coordinates labeled. Scale bar, 1 mm. (c) Energy mapping of the array prior to whisker deflection. (d) Energy mappings of the array immediately following the whisker deflection. (e) Signal waveform graphs collected from various locations.

isolating the OECT channels. The spin-coating speed was set to 2500 rpm, with a duration of 45 seconds. Subsequently, reactive ion etching (RIE) was conducted using O_2/SF_6 plasma at a power of 210 W, with gas flows of 90 sccm for O_2 and 3.5 sccm for SF_6, achieving an etch rate of 105 s μm^{-1}. This process was executed to expose the contact pads and the cross-section of the source and drain electrodes, using the RIE150-1/EXW (Exwell) system. Before etching, AZ10XT (Kayaku Advanced Materials) was spin-coated with 300 rpm for 4 s followed by 2000 rpm for 60 s, soft baked at 110 °C for 3 min, exposed with a dose of 90 mJ cm^{-2}, and developed for 7 min as the photoresist etching mask. The PEDOT:PSS films were prepared by blending 5 mL of an aqueous dispersion of PEDOT:PSS (PH1000, with a PEDOT:PSS weight ratio of 1 : 2.5) with 250 μL of ethylene glycol (98%, Macklin), 0.1 vol% of DMSO to enhance the conductivity, and 1 wt% of GOPS utilized as a crosslinker. The resulting dispersion was filtered using a 0.22 μm polytetrafluoroethylene filter and then spin-coated at 3000 rpm for 60 s. Subsequently, the film was baked at 100 °C on a hot plate for 1 minute and then the sacrificial layer was peeled off. Following this, the films underwent further baking at 140 °C for 1 hour and were immersed in DI water to eliminate any residual low-molecular weight compounds.

All the device performance measurements, including output and transfer curves, and pulse measurement for calculating response time, were carried out under ambient conditions in 0.01 M PBS (Sigma-Aldrich) of pH 7.4. An Ag/AgCl pellet (Warner Instruments) was used as the gate electrode. Keithley 4200 Semiconductor parameter analyzer was used to bias the transistor and record the drain and gate currents. All voltages were referenced to the source electrode kept at ground. In the long-term stability test, the fabricated devices were stored either in air or in PBS. Each test involved evaluating eight channels from the same device substrate.

Open Access Article. Published on 20 2025. Downloaded on 27.02.2026 08:34:30. This article is licensed under a Creative Commons Attribution-NonCommercial 3.0 Unported Licence.

Recording system setup

For multiplexed data acquisition, a custom electronic circuit was meticulously engineered. This customized circuit encompasses five primary elements, as illustrated in Fig. S4 (ESI†). The component displayed within the light blue box represents the switch matrix, constructed with ADG733BRUZ-REEL7, facilitating column cycling to accomplish multiplexing. The switching frequency of the switches is 2 kHz, corresponding to a sampling rate of 250 Hz for each line. All the 8 OECTs in each row were sampled simultaneously, yielding an effective sampling rate of 250 Hz per OECT. The content displayed within the light green box pertains to the *I*/*V* convertor to convert the drain source current signal into voltage by a transimpedance amplifier (1k gain) and then followed by a voltage follower. These components are implemented using TLC2201CD operational amplifiers. Subsequently, the signal is transmitted to the ADS1299 chip (red box) for analog-to-digital conversion. The content enclosed within the cyan box represents the Microcontroller Unit (MCU) STM32F103, responsible for controlling the switches of the switch matrix as well as managing data acquisition and transmission. The orange box represents the power supplies component, which provides the drain–source power supply to drive the operation of the transistor, as well as the power supply required for other circuit modules. The drain power supply was set to −1 V to ensure that the transistor achieves a transconductance of up to 3 mS even when the gate voltage is 0 V (Fig. S8, ESI†). Circuit board programming was performed using visual studio code. The configuration of the PXI system is shown in Fig. S13 (ESI†). Its data acquisition principle is similar to that of a circuit board. The sampling rate was tuned through the LabVIEW program. Here, data acquisition, demultiplexing, storage, and real-time display were conducted utilizing custom LabVIEW (National Instruments). All acquired data were stored for subsequent offline filtering and analysis utilizing custom MATLAB software provided by MathWorks.

In vivo evaluation

All experimental protocols have received ethical approval from the Committee on Animal Care at Tsinghua University and the Institutional Animal Care and Use Committee (IACUC) at Shenzhen Institute of Advanced Technology, Chinese Academy of Sciences, adhering to the principles outlined in the Guide for Care and Use of Laboratory Animals. The study protocol was also thoroughly reviewed and approved by the ethical committee of Tsinghua Shenzhen International Graduate School, Tsinghua University (approval number 2023-F121).

The C57BL/6 mice were procured from Guangdong Provincial Center for Laboratory Animals and housed under controlled environmental conditions, specifically maintained at a temperature of 23 °C and subjected to a 12-hour light/dark cycle. Food and water were available *ad libitum*. Several male mice with a weight range of 18–22 g were used in this study. Mice were anesthetized and maintained with isoflurane through a trachea inserted into the mouth of the mice. During the surgical procedure, the mice were securely immobilized in a stereotaxic apparatus. Subsequently, the fur covering the cranial region was eliminated using depilatory cream. Following the administration of anaesthesia for a duration of 10 to 15 minutes, the mice reached a state of profound anaesthesia. At this juncture, the scalp of the mice were meticulously excised using sterilized surgical scissors to reveal the cranial bones. Surgical implantation of two miniature stainless-steel screws was performed on the cranial bones directly above the cerebellum, designated to serve as ground and reference electrodes correspondingly. Two bilateral craniotomies were meticulously conducted with a hand-held electric drill, with each cranial aperture measuring 3 × 5 mm^2. These surgical interventions were executed on the right and left hemispheres of the cerebral cortex, respectively, situated superior to the somatosensory cortex. Specifically, the central coordinates of the craniotomy in the right hemisphere were designated at −4 mm along the antero-posterior axis and −2 mm along the medio-lateral axis, with reference to Bregma point. Symmetrically, the centre of the craniotomy in the left hemisphere mirrored the coordinates relative to the right hemisphere. The dura mater was excised, and the cortical surface underwent irrigation with saline solution (0.9%). Subsequently, 0.1 mL of a 100 mM bicuculline solution was administered onto a cotton ball, which was then positioned on the cortical surface for a duration of 5 minutes, facilitating the diffusion of bicuculline effects through the cortical layers to induce epilepsy.[11,46] The bicuculline (98%, Aladdin) was first dissolved in dimethyl sulfoxide (99.5%, Xilong Scientific) to a concentration of 1 mM, and then diluted with physiological saline to obtain a 0.1 mM solution. Following the 5-minute interval, the cotton ball was extracted, and the vOECT array, alongside the commercial passive Pt electrode array (NeuroNexus; E32-300-20-50), was gradually descended onto the left and right hemispheres of the cerebral cortex, respectively as shown in Fig. 3a. In contrast to the custom-designed vOECT array utilized in this study, the NeuroNexus represents a passive ECoG array featuring 32 electrodes organized into 4 columns and 8 rows, with a contact spacing of 300 mm and a contact diameter measuring 50 mm. Given the high flexibility, the OECT array could softly and intimately laminate onto the brain without trauma. The commercial Pt electrodes array was connected to the Intan recording system through the H32 ECoG Connector with the sampling rate of 30 kHz. The OECT array was accessed *via* a zero-insertion force (ZIF) connector with flat flexible cable to our custom-built circuit board, which operated at a sampling rate of 250 Hz. Utilizing a PXI setup, a 16 × 16 section of the high-density array was selected for signal mapping. The sampling frequencies were set at 250 Hz for capturing epileptic signals and 625 Hz for whisker-related signals, ensuring adequate resolution for the respective signal characteristics.

For chronic signal recording, a male C57BL/6 mouse with a weight of 20 g was used. We fixed a homemade cap made from a centrifuge tube to the skull using dental cement after craniotomy removal of dura mater as shown in Fig. S11a (ESI†). This cap is used to store the array and the ground wire. Then, the vOECT array is attached to the scalp and sealed with

 This journal is © The Royal Society of Chemistry 2025

Open Access Article. Published on 20 2025. Downloaded on 27.02.2026 08:34:30. This article is licensed under a Creative Commons Attribution-NonCommercial 3.0 Unported Licence.

biological glue and dental cement. Finally, the cap is closed and sealed with parafilm (Fig. S11b, ESI†) to ensure that the mouse can move freely without damaging the device. After surgery, the mouse was housed individually in cage with food and water provided *ad libitum*. During testing, the cap is opened again, and the device is connected to an adapter board *via* a ZIF connector and to the backend acquisition circuit board through a flexible flat cable (Fig. S11c, ESI†). Subsequently, seizures were induced by intraperitoneal injection of 0.5 mL of 100 mM bicuculline solution, the same solution used in acute *in vivo* recordings.

Cytotoxicity

For cytotoxicity test, the extract dilution methods were used with murine hippocampal neuronal HT22 cells. The vOECT array is used as a target sample, with the bare HT22 medium as the control group. The vOECT arrays were extracted in culture media for 24 h incubation at 37 °C in 5% CO_2. The murine hippocampal neuronal HT22 cells and HT22 medium were purchased from Procell Life Science & Technology Company (Wuhan). The collected murine hippocampal neuronal HT22 cells were then plated in 48-well microculture plates in complete extract culture medium. At day 1 and day 5 *in vitro*, the cells were stained with Calcein-AM/PI Cell Viability/Cytotoxicity Assay Kit (Beyotime). The cell morphology were observed with a fluorescence microscope (DMi8, Leica). For CCK-8 assay, the fresh culture medium was added to obtain the extracts with different concentrations: 100%, 50%, 25%, 13%, 7%, and 4% following the calculation $100 \times \frac{1}{2} = 50\%$, *i.e.*, 30 μL of 100% extract in 60 μL of culture medium; $50 \times \frac{1}{2} = 25\%$, *i.e.*, 30 μL of 50% extract in 60 μL of culture medium, *etc.* After the cells had been seeded at a density of 5.0×10^4 cells per well into a 96-well plate in duplicate and incubated at 37 °C for 24 h, the medium was replaced with the diluted extracts at six different concentrations and a bare HT22 medium as control group. The cells were then incubated for a further 1 and 5 days at 37 °C in a humidified atmosphere containing 5% carbon dioxide. At day 1 and day 5, each well was stained with CCK-8 solution (APExBIO, America). The viability of the cell cultures of each well was measured using the microplate reader (TECAN Infinite 200 Pro) Relative cell viability was defined as the percentage of the optical density of a diluted extract containing medium to the optical density of the corresponding non-treated control.

Immunohistochemistry

We implanted the sensing part of the probe in the brain of 18–20 g mice. A 1.5×1.5 mm^2 craniotomy was conducted in the right hemisphere above the somatosensory cortex. The dura mater was retracted, and the sensing part of the array was slowly lowered on the surface of the cortex. Three cranial nails were nailed to the skull to better hold the dental cement in place. The skull and OECT platform were then covered with biological glue and dental cement. After 12 weeks, the mice were deeply anesthetized by intraperitoneal injection of pentobarbital sodium solution and perfused and fixed using a fixative solution containing 4% paraformaldehyde (PFA, Beyotime) in phosphate-buffered saline (PBS, Beyotime), pH 7.4. The mice received 300 mL of this fixative per 100 g of body weight. After perfusion, the brains were removed from the skull, kept in PFA for 24 hours at 4 °C, then post-fixed in a solution of 30% sucrose solution in (0.01 M PBS) for 48 hours at 4 °C. The dehydrated brains were frozen in Optimal Cutting Temperature compound (OCT, Sakura), and brain slices (40 μm) containing the somatosensory cortex were sectioned coronally using a cryostat (Leica, CM1950). After washing three times with PBS, the brain slices were blocked with 5% BSA and 0.3% Triton X-100 for 2 hours at room temperature. Subsequently, the slices were incubated overnight at 4 °C with primary antibodies (anti-IBA1, 1 : 1000, rabbit, Invitrogen; anti-GFAP, 1 : 300, IgG1, Cell Signalling) diluted in PBST (0.3% Triton X-100) to label microglia and astrocytes. Following five washes for 10 minutes each in PBST, the slices were incubated with secondary antibodies (1 : 1000, Alexa Fluor 555, Alexa Fluor 633) for 2 hours at room temperature. After two additional washes for 10 minutes each in PBST, the slices were incubated for 10 minutes at room temperature with DAPI (to label nuclei) and washed three times with PBST. Finally, the sections were mounted and imaged using a confocal microscope (SP5, Leica). Images were analyzed using the image-processing software ImageJ (NIH). Raw fluorescence intensity values of every pixel in a ROI were averaged and then normalized to the ROI area (mean intensity mm^{-2}). Neuronal density was calculated using the ITCN plugin of ImageJ (NIH). Neurons inside ROIs were counted on images of NeuroTrace stained slices.

Author contributions

Xiaomin Xu conceived the topic and supervised the research. Wei Xu and Yanlan Zhu designed the device structure, fabricated the ultraflexible vOECT arrays, and performed the analysis. Xiaolin Zhou, Haoyue Guo, and Jingxin Wang designed the backend recording system. Ruiqi Zhu and Xing Ma performed biocompatibility test. Zhengwei Hu and Xiaojian Li measured neural signal and assisted in the signal analysis. Wei Ma and Xing Ma discussed and revised the manuscript. Wei Xu, Yanlan Zhu, and Xiaomin Xu wrote the manuscript. All authors discussed and revised the manuscript.

Data availability

The data supporting this article have been included as part of the ESI.†

Conflicts of interest

There are no conflicts to declare.

Acknowledgements

The authors acknowledge support from Ministry of Science and Technology of the People's Republic of China (National Key R&D Program of China, no. 2023YFE0101400), National Natural Science Foundation of China (no. 52273249), Natural Science Fund

of Guangdong Province-General Project (no. 2021ZT09L197), Shenzhen Science and Technology Innovation Committee—Outstanding Youth Basic Research Project (RCYX20210609103710028) and Shenzhen High-level Talent Team Project (KQTD20210811090112002).

Open Access Article. Published on 20 2025. Downloaded on 27.02.2026 08:34:30. This article is licensed under a Creative Commons Attribution-NonCommercial 3.0 Unported Licence.

Notes and references

1 F. A. C. Azevedo, L. R. B. Carvalho, L. T. Grinberg, J. M. Farfel, R. E. L. Ferretti, R. E. P. Leite, W. J. Filho, R. Lent and S. Herculano-Houzel, *J. Comput. Neurol.*, 2009, **513**, 532–541.
2 K. Roy, A. Jaiswal and P. Panda, *Nature*, 2019, **575**, 607–617.
3 W. M. Y. Mohamed, B. S. Alghamdi and A. Alexiou, *Front. Neurosci.*, 2023, **17**, 1–3.
4 P. Konrad and T. Shanks, *Neurobiol. Dis.*, 2010, **38**, 369–375.
5 R. Hultman, K. Ulrich, B. D. Sachs, C. Blount, D. E. Carlson, N. Ndubuizu, R. C. Bagot, E. M. Parise, M.-A. T. Vu, N. M. Gallagher, J. Wang, A. J. Silva, K. Deisseroth, S. D. Mague, M. G. Caron, E. J. Nestler, L. Carin and K. Dzirasa, *Cell*, 2018, **173**, 166–180.e114.
6 H. S. Kaplan, O. Salazar Thula, N. Khoss and M. Zimmer, *Neuron*, 2020, **105**, 562–576.e569.
7 A. R. Wyler, G. A. Ojemann, E. Lettich and A. A. Ward, Jr., *J. Neurosurg.*, 1984, **60**, 1195–1200.
8 K. J. Miller, D. Hermes and N. P. Staff, *Neurosurg. Focus*, 2020, **49**, E2.
9 H. Moon, J. Kwon, J. Eun, C. K. Chung, J. S. Kim, N. Chou and S. Kim, *Adv. Mater. Technol.*, 2024, **9**, 2301692.
10 M. Wu, K. Yao, N. Huang, H. Li, J. Zhou, R. Shi, J. Li, X. Huang, J. Li, H. Jia, Z. Gao, T. H. Wong, D. Li, S. Hou, Y. Liu, S. Zhang, E. Song, J. Yu and X. Yu, *Adv. Sci.*, 2023, **10**, 2300504.
11 D. Khodagholy, T. Doublet, P. Quilichini, M. Gurfinkel, P. Leleux, A. Ghestem, E. Ismailova, T. Herve, S. Sanaur, C. Bernard and G. G. Malliaras, *Nat. Commun.*, 2013, **4**, 1575.
12 S. Cheng, R. Zhu and X. Xu, *Commun. Mater.*, 2024, **5**, 99.
13 T. Someya, Z. Bao and G. G. Malliaras, *Nature*, 2016, **540**, 379–385.
14 J. Rivnay, H. Wang, L. Fenno, K. Deisseroth and G. G. Malliaras, *Sci. Adv.*, 2017, **3**, e1601649.
15 J. Viventi, D.-H. Kim, L. Vigeland, E. S. Frechette, J. A. Blanco, Y.-S. Kim, A. E. Avrin, V. R. Tiruvadi, S.-W. Hwang, A. C. Vanleer, D. F. Wulsin, K. Davis, C. E. Gelber, L. Palmer, J. Van der Spiegel, J. Wu, J. Xiao, Y. Huang, D. Contreras, J. A. Rogers and B. Litt, *Nat. Neurosci.*, 2011, **14**, 1599–1605.
16 L. Muller, L. S. Hamilton, E. Edwards, K. E. Bouchard and E. F. Chang, *J. Neural Eng.*, 2016, **13**, 056013.
17 E. Boran, G. Ramantani, N. Krayenbühl, M. Schreiber, K. König, T. Fedele and J. Sarnthein, *Clin. Neurophysiol.*, 2019, **130**, 1882–1888.
18 T. Kaiju, K. Doi, M. Yokota, K. Watanabe, M. Inoue, H. Ando, K. Takahashi, F. Yoshida, M. Hirata and T. Suzuki, *Front. Neural Circuits*, 2017, **11**, 1–13.
19 G. Gholmieh, W. Soussou, M. Han, A. Ahuja, M. C. Hsiao, D. Song, A. R. Tanguay, Jr. and T. W. Berger, *J. Neurosci. Methods*, 2006, **152**, 116–129.
20 G. Buzsáki, C. A. Anastassiou and C. Koch, *Nat. Rev. Neurosci.*, 2012, **13**, 407–420.
21 K. H. Pettersen, A. Devor, I. Ulbert, A. M. Dale and G. T. Einevoll, *J. Neurosci. Methods*, 2006, **154**, 116–133.
22 G. Buzsáki and A. Draguhn, *Science*, 2004, **304**, 1926–1929.
23 C. Cea, G. D. Spyropoulos, P. Jastrzebska-Perfect, J. J. Ferrero, J. N. Gelinas and D. Khodagholy, *Nat. Mater.*, 2020, **19**, 679–686.
24 G. D. Spyropoulos, J. N. Gelinas and D. Khodagholy, *Sci. Adv.*, 2019, **5**, eaau7378.
25 J. Kawahara, P. A. Ersman, K. Katoh and M. Berggren, *IEEE Trans. Electron Devices*, 2013, **60**, 2052–2056.
26 M. J. Donahue, A. Williamson, X. Strakosas, J. T. Friedlein, R. R. McLeod, H. Gleskova and G. G. Malliaras, *Adv. Mater.*, 2018, **30**, 1705031.
27 R. B. Rashid, W. Du, S. Griggs, I. P. Maria, I. McCulloch and J. Rivnay, *Sci. Adv.*, 2021, **7**, eabh1055.
28 M. Abarkan, A. Pirog, D. Mafilaza, G. Pathak, G. N'Kaoua, E. Puginier, R. O'Connor, M. Raoux, M. J. Donahue, S. Renaud and J. Lang, *Adv. Sci.*, 2022, **9**, 2105211.
29 D. A. Koutsouras, F. Torricelli and P. W. M. Blom, *Adv. Electron. Mater.*, 2023, **9**, 2200868.
30 W. Huang, J. Chen, Y. Yao, D. Zheng, X. Ji, L.-W. Feng, D. Moore, N. R. Glavin, M. Xie, Y. Chen, R. M. Pankow, A. Surendran, Z. Wang, Y. Xia, L. Bai, J. Rivnay, J. Ping, X. Guo, Y. Cheng, T. J. Marks and A. Facchetti, *Nature*, 2023, **613**, 496–502.
31 J. Kim, R. M. Pankow, Y. Cho, I. D. Duplessis, F. Qin, D. Meli, R. Daso, D. Zheng, W. Huang, J. Rivnay, T. J. Marks and A. Facchetti, *Nat. Electron.*, 2024, **7**, 234–243.
32 S. Xu, Y. Zhang, J. Cho, J. Lee, X. Huang, L. Jia, J. A. Fan, Y. Su, J. Su, H. Zhang, H. Cheng, B. Lu, C. Yu, C. Chuang, T.-I. Kim, T. Song, K. Shigeta, S. Kang, C. Dagdeviren, I. Petrov, P. V. Braun, Y. Huang, U. Paik and J. A. Rogers, *Nat. Commun.*, 2013, **4**, 1543.
33 Y. Jimbo, D. Sasaki, T. Ohya, S. Lee, W. Lee, F. Arab Hassani, T. Yokota, K. Matsuura, S. Umezu, T. Shimizu and T. Someya, *Proc. Natl. Acad. Sci. U. S. A.*, 2021, **118**, e2022300118.
34 R. Garcia-Cortadella, G. Schwesig, C. Jeschke, X. Illa, A. L. Gray, S. Savage, E. Stamatidou, I. Schiessl, E. Masvidal-Codina, K. Kostarelos, A. Guimerà-Brunet, A. Sirota and J. A. Garrido, *Nat. Commun.*, 2021, **12**, 211.
35 R. Garcia-Cortadella, N. Schäfer, J. Cisneros-Fernandez, L. Ré, X. Illa, G. Schwesig, A. Moya, S. Santiago, G. Guirado, R. Villa, A. Sirota, F. Serra-Graells, J. A. Garrido and A. Guimerà-Brunet, *Nano Lett.*, 2020, **20**, 3528–3537.
36 W. Lee, S. Kobayashi, M. Nagase, Y. Jimbo, I. Saito, Y. Inoue, T. Yambe, M. Sekino, G. G. Malliaras, T. Yokota, M. Tanaka and T. Someya, *Sci. Adv.*, 2018, **4**, eaau2426.
37 W. Lee, D. Kim, N. Matsuhisa, M. Nagase, M. Sekino, G. G. Malliaras, T. Yokota and T. Someya, *Proc. Natl. Acad. Sci. U. S. A.*, 2017, **114**, 10554–10559.
38 W. Lee, D. Kim, J. Rivnay, N. Matsuhisa, T. Lonjaret, T. Yokota, H. Yawo, M. Sekino, G. G. Malliaras and T. Someya, *Adv. Mater.*, 2016, **28**, 9722–9728.
39 X. Gu, C. Yao, Y. Liu and I.-M. Hsing, *Adv. Healthcare Mater.*, 2016, **5**, 2345–2351.

 This journal is © The Royal Society of Chemistry 2025

Open Access Article. Published on 20 2025. Downloaded on 27.02.2026 08:34:30.
This article is licensed under a Creative Commons Attribution-NonCommercial 3.0 Unported Licence.

40 K. Im, J.-M. Lee, O. Lyttelton, S. H. Kim, A. C. Evans and S. I. Kim, *Cereb. Cortex*, 2008, **18**, 2181–2191.
41 D. A. Bernards and G. G. Malliaras, *Adv. Funct. Mater.*, 2007, **17**, 3538–3544.
42 M. Shokoueinejad, D.-W. Park, Y. H. Jung, S. K. Brodnick, J. Novello, A. Dingle, K. I. Swanson, D.-H. Baek, A. J. Suminski, W. B. Lake, Z. Ma and J. Williams, *Micromachines*, 2019, **10**, 62.
43 R. Oostenveld, D. F. Stegeman, P. Praamstra and A. van Oosterom, *Clin. Neurophysiol.*, 2003, **114**, 1194–1202.
44 S. Chatterjee, T. Sakorikar, A. Bs, R. K. Joshi, A. Sikaria, M. Jayachandra, V. V and H. J. Pandya, *Biomed. Microdevices*, 2022, **24**, 31.
45 A. Zouhar, P. Mare, K. Lišková-Bernášková and M. Mudrochová, *Epilepsia*, 1989, **30**, 501–510.
46 K. J. Yu, D. Kuzum, S.-W. Hwang, B. H. Kim, H. Juul, N. H. Kim, S. M. Won, K. Chiang, M. Trumpis, A. G. Richardson, H. Cheng, H. Fang, M. Thompson, H. Bink, D. Talos, K. J. Seo, H. N. Lee, S.-K. Kang, J.-H. Kim, J. Y. Lee, Y. Huang, F. E. Jensen, M. A. Dichter, T. H. Lucas, J. Viventi, B. Litt and J. A. Rogers, *Nat. Mater.*, 2016, **15**, 782–791.
47 S. Arroyo and S. Uematsu, *J. Clin. Neurophysiol.*, 1992, **9**, 441–448.
48 W. Lee, D. Kim, N. Matsuhisa, M. Nagase, M. Sekino, G. G. Malliaras, T. Yokota and T. Someya, *Proc. Natl. Acad. Sci. U. S. A.*, 2017, **114**, 10554–10559.
49 S. Crochet and C. C. H. Petersen, *Nat. Neurosci.*, 2006, **9**, 608–610.
50 V. Sreenivasan, V. Esmaeili, T. Kiritani, K. Galan, S. Crochet and C. C. H. Petersen, *Neuron*, 2016, **92**, 1368–1382.